

# Development of a Flash X-Ray Radiography and Tomography System to Measure Bone Mineral Density

John F. Seely

[john.seely@nrl.navy.mil](mailto:john.seely@nrl.navy.mil), Tel. 202-767-3529, Fax 202-404-7997

Naval Research Laboratory, Code 7674, Washington, DC 20375-5352

Craig N. Boyer

Praxis Inc., 2200 Mill Road 5th Floor, Alexandria , Virginia 22314

[cboyer@ssd5.nrl.navy.mil](mailto:cboyer@ssd5.nrl.navy.mil)

Glenn E. Holland

Sachs Freeman Associates Inc., 9315 Largo Drive West Suite 200, Largo, MD 20774

[gholland@ssd5.nrl.navy.mil](mailto:gholland@ssd5.nrl.navy.mil)

**Final Report for Project T-5282W. 21 February 2003**

**Naval Research Laboratory, Space Science Division, Code 7674, Washington DC 20024**

## Introduction

This project addresses the NASA need for a relatively compact and portable x-ray system to perform bone mineral density studies on the International Space Station. The use of a 60 ns x-ray pulse to image biological specimens has been successfully demonstrated. With the dual-energy flash source, there is no need to change the anode-cathode (AK) voltage since the applied voltage across the AK gap is effectively swept during operation. The x-ray energy is high early in the pulse and lower later in the pulse. Utilizing the dual-energy properties of the x-ray source to perform x-ray absorptometry without changing the applied voltage across the AK gap or changing filters simplifies the implementation of the source. A computer simulation model was developed for the x-ray source, which permitted the distribution of radiated energy in a plane normal to the symmetry axis of the x-ray anode to be determined as well as its spectrum. The use of two amorphous silicon (aSi) imaging panels stacked in tandem with a metal x-ray filter yielded both hard and soft x-ray images. X-ray assays of bone mineral density (BMD) to accuracies of 2% percent are possible when the attenuation of the soft tissue is removed by means of a subtraction algorithm and by using a calibration phantom. The dual-energy x-ray absorptometry (DEXA) project implemented a complete system that integrates the dual-energy pulsed x-ray source with the aSi digital imaging panels. Experiments were performed to determine the distribution of radiation over the image plane and the sensitivity or modulation transfer function of the imaging panels. Based on the imaging experiments and the ability of the software to generate computed tomographic (CT) images, a decision was made to add CT capability to DEXA imaging so that a 3-D map of the site bone mineral density could be obtained. The addition of the CT capability increases the patient radiation dose, so image-based reconstruction was planned for the purpose of reducing the dose. In this process a limited number (3 to 5) images of a target site are processed using *a priori* knowledge of the site architecture to construct a CT image. The questions that were answered in a positive way during this project were as

follows: Is the fluence, forward distribution, repeatability, and energy spectrum of the pulsed x-ray source sufficient? Will the sensitivity of the aSi digital imaging panels and the choice of conversion phosphor produce an image suitable for DEXA analysis? Will the DEXA software operate correctly, and is it capable of generating a 3D map of bone mineral density?

## **Materials and Methods**

### **Dual Energy X-Ray Absorptometry (DEXA) System**

Figure 1 shows a perspective view generated from the 3-D CAD model of the mechanical subsystem for the DEXA system. The entire mechanical system can be placed on a table. The mechanical subsystem design incorporates three computer-controlled axes and two adjustable mounting axes for a total of five degrees of freedom. The X and Y-axes are used to position the object in front of the two dpiX Flash Scan 30/33 detectors, and the R axis is used to rotate the object. The X and Y-axes employ IDC linear slides with 50  $\mu\text{m}$  resolution, and the R axis employs an IDC rotary table with 0.001° resolution. All three axes are driven by high-resolution stepper motors from a Galil DMC-2140 motion controller. The interface between the Galil and the controlling Microsoft Windows 2000 computer is via fiber optic. Communication is via Ethernet utilizing the TCP/IP protocol. The Z direction (i.e., the object-to-detector distance) is adjusted and set by relocating the detector and/or X-Y-R manipulator on the 30"x30" optical breadboard, which serves as the base for the mechanical subsystem. The spacing between holes on the optical breadboard is 0.5". The source-to-detector distance is adjusted and set by physically moving the X-ray tube with respect to the entire mechanical subsystem (these two subsystems are not mechanically coupled).

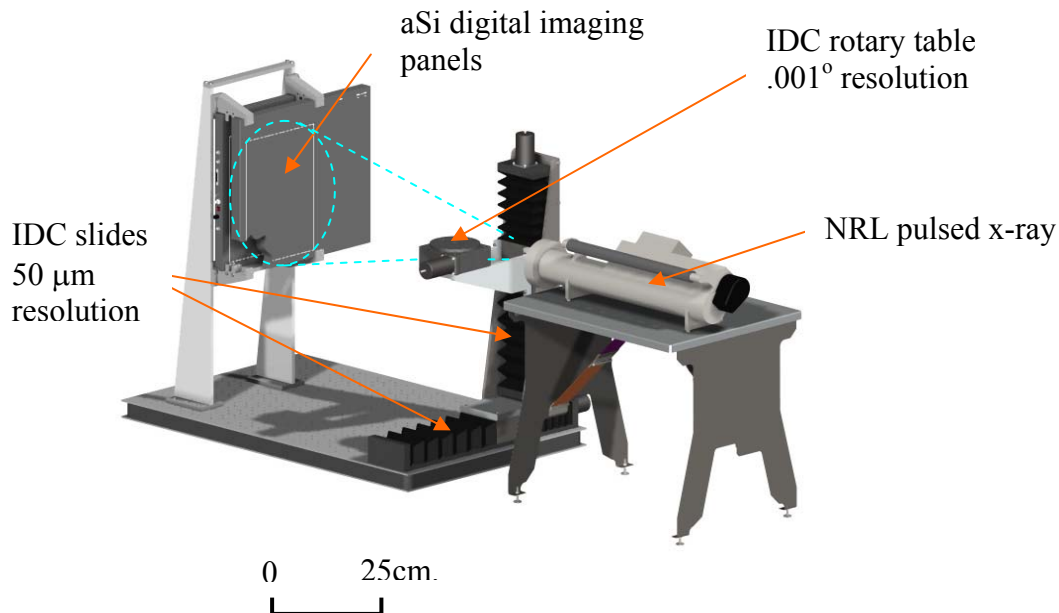


Fig. 1. Perspective view of the NRL DEXA system.

## Imaging Processing

Figures 2 and 3 identify the various components of the electronic control system for the computed DEXA system (CDEX). All of the computer hardware (except monitor, keyboard and mouse) is mounted in a 19" EIA equipment rack incorporated within metal shipping containers. Due to the height and weight of the equipment, the hardware was split between two rack mount shipping containers (each 9 rack units high) to meet United Parcel Service shipping limits. The lower container has casters and the upper container has latches, which physically secure the upper container to the lower container during setup. Both containers have removable front and rear covers for access to the hardware and to promote acceptable airflow. The DEXA system utilizes two computers which each have dual Pentium III 1 GHz processors, 1 GB RAM, dual-head Matrox G450 video adapters running OpenGL, and 100-Base-T network interface cards (NICs). Additionally, the primary computer has a 100-Base-F (fiber optic) NIC for communications with the Galil motion controller. A single 17.4" flat-panel monitor, keyboard, and mouse are used to operate both the primary and secondary computers through a Keyboard-Video-Mouse (KVM) switch. Other components of the CDEX computer system include a 160 GB RAID 5 data server, 10/100 Ethernet switch, and un-interruptible power supply (UPS). A 3 rack unit high filler plate covers an expansion slot for future hardware needs.

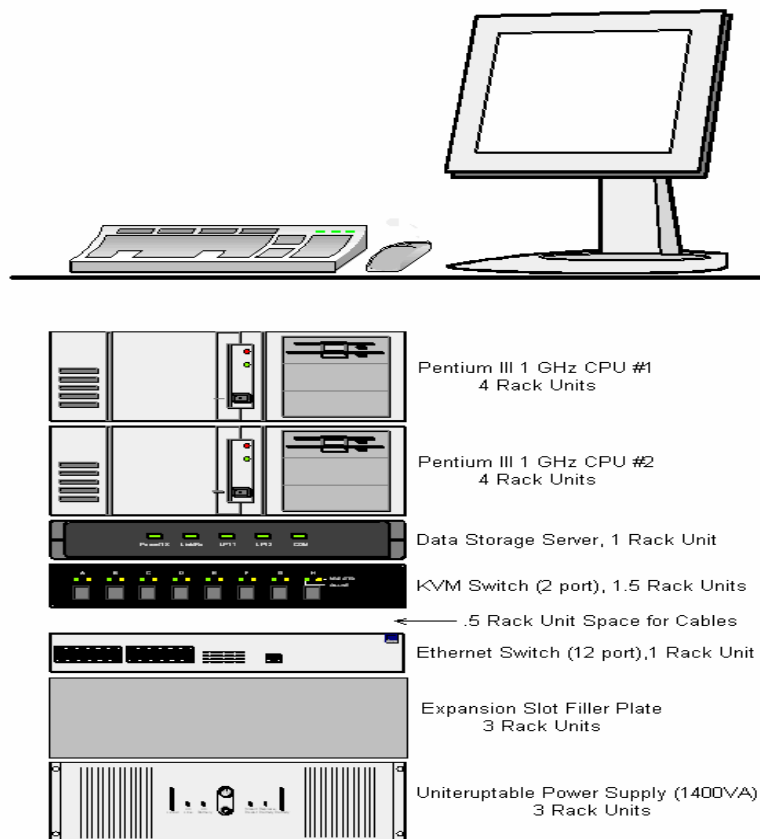


Fig. 2. The DEXA image processor architecture.

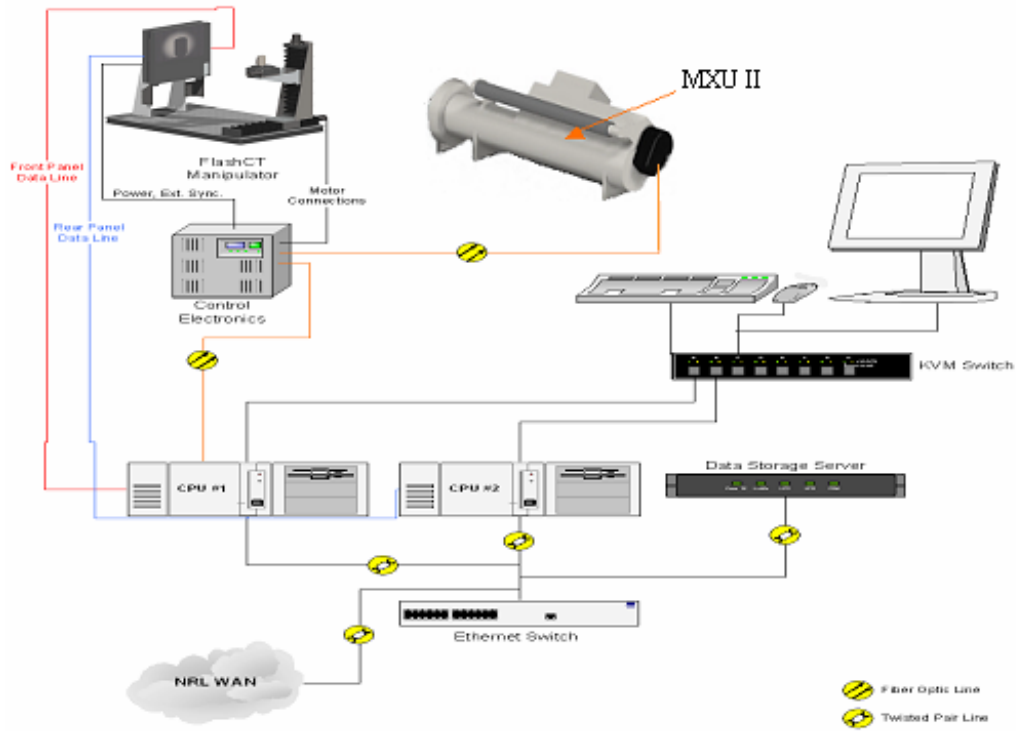


Fig. 3. NRL DEXA system.

Figure 3 shows the layout of the entire DEXA system. Data is moved through the system via TCP/IP packets on a 100-Base-T Ethernet Local Area Network (LAN). Both computers and the data server are attached to a LAN switch, which directs traffic to the appropriate address (as opposed to a LAN hub which broadcasts data out to all attached computers). The LAN switch can also be connected to a Wide Area Network (WAN) for transmitting data via e-mail. Each computer controls one of the two dpiX Flash Scan 30/33 detectors. The computers operate in client-server mode with the primary computer (CPU #1) acting as the server and the secondary computer (CPU #2) acting as the client. The server is responsible for synchronizing data acquisition between the two computers. CPU #1 is additionally connected to the Galil controller and is responsible for synchronizing motion control and x-ray generation with data acquisition. The x-ray tube (MXU II in Fig. 3) is fiber optically coupled to the controller electronics box. Fiber optics were implemented to isolate the large electromagnetic pulse generated by the x-ray source from the computer control system. Internally, the Galil interfaces with the x-ray tube through a TTL-to-Fiber converter. TTL signals are sent from the Galil to the converter and then from the converter to the x-ray tube. External synchronization of the Flash Scan detectors is utilized to ensure precise capture of the short radiation pulse generated by the x-ray tube and is accomplished via TTL signals derived within the Galil.

### Flash X-Ray Source

The flash x-ray source was developed and experimentally characterized by numerically solving Langmuir's equation for one-dimensional space charge limited (SCL) flow in cylindrical geometry. This solution was coupled to a circuit model for the Marx impulse

generator. Langmuir's solution for nonrelativistic SCL flow of electron current across the AK gap in a cylindrical x-ray diode can be written

$$I_{SCL} = m_e c^3 / e (2^{3/2} W_c / 9 R_A \kappa^2) U^{3/2} \quad (1)$$

where  $R_A$  is the anode radius,  $\kappa^2$  is a function of the ratio of the cathode and anode radii ( $R_C/R_A$ ),  $U = eV/m_e c^2$ , and  $V$  is the anode-cathode potential. While the above equation does not include an expression for the expansion of a virtual cathode sheath across the anode-cathode gap, it can be included. Cathode plasma has been experimentally observed to expand isentropically at constant velocity, and therefore its movement can be modeled by decreasing the cathode radius with time so that it approaches the anode. Using the cross sectional drawing shown in Fig. 4, a simplified model of the x-ray tube's anode-cathode was constructed.

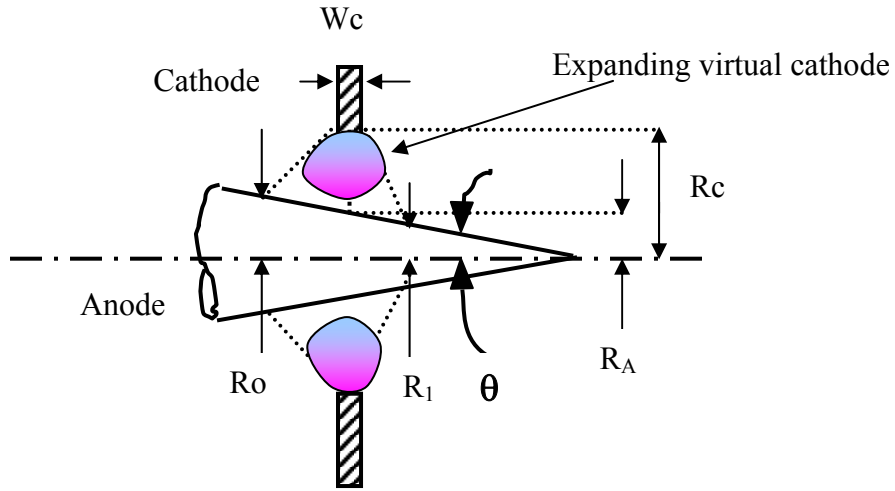


Fig. 4. Model used to describe the expansion of the cathode plasma sheath (virtual cathode) into the vacuum region between the AK gap.

The neutral plasma, the colored (shaded) region shown in Fig. 4, leaves the cathode surface and expands at constant velocity  $V_{cp}$  toward the anode. Since the plasma expands isentropically, its width can be approximated as

$$W_c(t) = W_c + 2tV_{cp} \quad (2)$$

where  $t$  is the time since formation of cathode plasma and  $W_c$  is the initial width of the emitting cathode. The time dependence of the cathode radius can be expressed by

$$R_c(t) = R_c - tV_{cp} \quad (3)$$

As the cathode width increases, the anode-cathode gap decreases and large currents of electrons can flow toward the anode. Substitution of Eq. (2) and Eq. (3) into Eq. (1) completes the diode model. This model can now be coupled to the equivalent circuit for

the Marx impulse generator and the model that describes the behavior of the Marx capacitors.

### Marx Impulse Generator

Previous circuit models developed early in the project contained  $n-1$  loops coupled through  $n$  shared energy storage capacitors and required a time dependent solution in each loop. Rather than use such a complex circuit model to find the charge flowing into x-ray tube, a simpler model was developed. Results from our  $n-1$  loop circuit model showed that individual circuit elements do not strongly control the current and voltage across the x-ray tube AK gap but rather the time delay between the Marx trigger and the arrival of the high voltage pulse at the peaking switch. It is the lumped capacitance, inductance, and spark gap resistance of the Marx generator that control the AK potential and the cathode current.

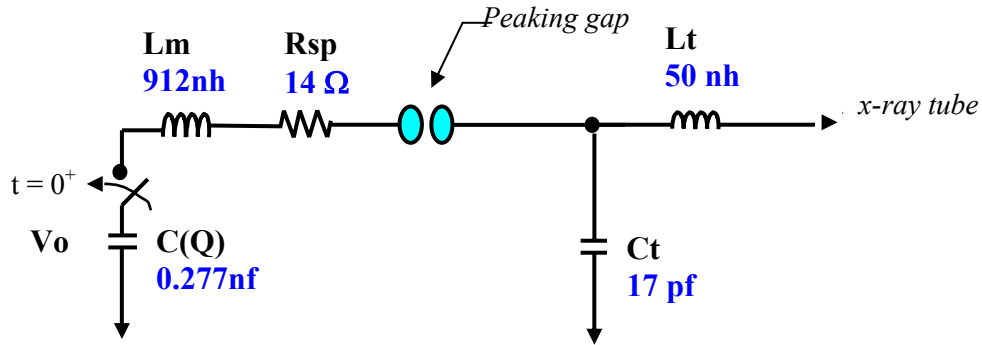


Fig 5. The lumped element equivalent circuit of the Marx impulse generator when coupled through the peaking gap to the anode of the x-ray tube.

The self consistent solution for the current and voltage in the x-ray tube was obtained by solving for the currents and charges in the two loop circuit of Fig. 5. In this circuit, the x-ray tube acts as a complex impedance which controls the current in the second loop. The time-dependent current and charge in each loop were obtained from a 4th order Runge Kutta solution of the coupled nonlinear second-order differential equations. As the solution time advances, Eq. (2) and Eq. (3) determine the width and radius of the virtual cathode and return these parameters to Eq. (1). Before running the model, the initial values  $R_c$ ,  $R_A$ ,  $W_c$ ,  $V_o$ , and  $\xi$  are specified. Additional parameters such as  $C_o$ ,  $L_m$ , and  $R_{sp}$  from Fig. 5 and  $\theta$  defined in Fig. 4 can be changed but are usually fixed throughout a series of runs.

### Comparison of Model Predictions with Experimental Current and Voltage

Two anode materials are used in our x-ray tube. The first is 80%W/20% Cu alloy (by weight), and the second is pure tungsten. Both anodes were right cylindrical cones having a  $36^\circ$  vertex angle. In the present x-ray tube, the tip of each anode extends just beyond and is concentric with the hole in the cathode.

The anode-cathode (AK) current and the AK voltage, measured using a 1 GHz bandwidth oscilloscope, were compared with their respective calculated values. A typical

simulation is presented in Fig. 6 with the following parameters: 3 mm thick graphite cathode with a 2.5 mm AK spacing. While the modeling predicts that a current of 1.6 kA flows from cathode to anode, the observed current is 2.2 kA. If equal numbers of ions and electrons are present in the anode-cathode gap, a factor of two increase in electron current should occur over all energies. While the electron current in the oscillogram of Fig. 6 is not twice the SCL value, it does exceed the SCL value and could be accounted for by a partial neutralization of the electron charge in the AK gap due to the presence of a counter flowing ion current. Production of ions from an anode plasma has been observed when the surface temperature rises to several hundred degrees Celsius. This is certainly the case for our anodes because the surface shows evidence of sputtering. In addition, the variation of the ratio ( $R_C/R_A$ ) when long cathodes are present is another variable that must be included in any SCL solution that attempts to deal with the actual AK geometry encountered in operating field emission tubes.

### 2.5 mm AK Gap

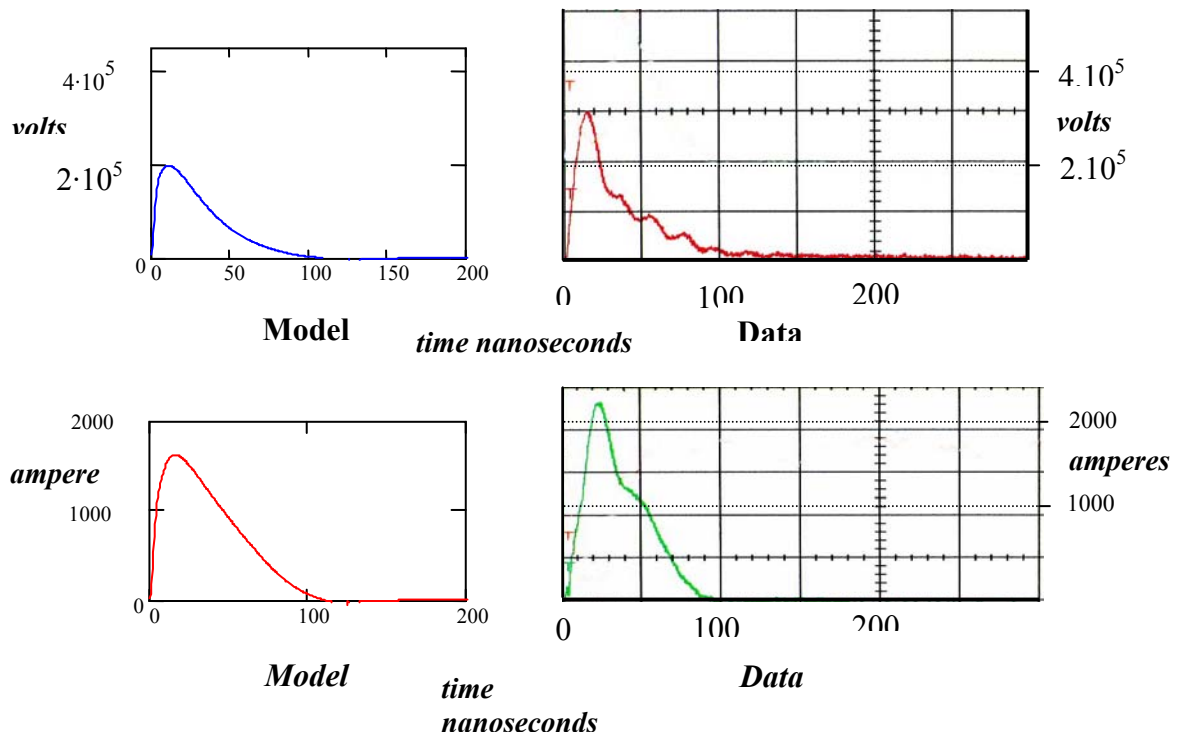


Fig. 6. Results derived from modeling the AK potential (top left) and the cathode current (bottom left) are compared to the oscillograms obtained from our field emission tube (right top and bottom).

### **Analysis of the X-Ray Pulse**

X-rays emitted from the tungsten anode were initially detected with a gated photomultiplier (PM) tube configured to use the first dynode as a photocathode with the tube's photocathode biased so that it did not produce photoelectrons. The PM tube was gated on by raising the dynode potential just before the x-ray pulse arrived. Because the dynodes in the PM tube are very thin, they convert only a fraction of the incoming hard x-ray photons to photoelectrons; the remainder of the photons escape without producing additional photoelectrons. For this reason, a quantitative measurement of the x-ray dose

as a function of energy was not made. However, time resolved x-ray pulse shapes were obtained so that pulses at different energies could be compared with the unfiltered pulse. With the PM detector placed 137 cm from the middle of the AK gap of the x-ray tube, three different filters were used to progressively harden the x-ray pulses. By comparing the filtered and unfiltered x-ray pulse with the AK potential, it was found that the full width at half maximum (FWHM) of the filtered x-ray pulse is very close to the FWHM of the AK potential for voltages >150 kV. The unfiltered x-ray pulse is therefore composed of a hard central pulse embedded within a broad pulse of much lower energy.

### **Delivered X-Ray Dose**

The radiated energy emitted from the field emission x-ray tube was measured using pocket dosimeters together with an ionization chamber. Measurements were conducted along the axis of rotational symmetry of the anode. Both filtered and unfiltered measurements were made with the Marx impulse generator charged to deliver 300 kV. The average unfiltered x-ray dose at 30.5 cm was 50 millirems. When the x-ray pulse was hardened by passage through a 0.127 mm thick tantalum foil, the recorded dose dropped to 2 millirems. Shot-to-shot reproducibility of the amplitude of the x-ray pulse was better than 95%.

### **Discrete Measurement of Emitted X-Ray Energy using Ross Filter Pairs**

The normalized fraction of x-ray energy delivered within selected energy bands was measured with a four-channel fast-scintillation detector as shown in Fig. 7. Each channel consisted of an ultraviolet sensitive photomultiplier tube (PMT) with its photocathode coupled to a 2 cm thick BaF<sub>2</sub> scintillator crystal through a UV band pass filter and a quartz condensing lens. Scintillator thickness was chosen so that x-ray photons up to 200 keV and 80% of all photons between 200 and 300 keV were stopped in the volume of the crystal. The purpose of the narrow bandpass UV filter, centered at 220 nm, was to permit only the fast scintillation light, with a decay time between 600 and 800 ps, to reach the PMT's photocathode. Foil filters were placed in front of three of the scintillator crystals, and the signals from these channels were normalized to the signal from the remaining unfiltered channel. For the measurements discussed below, one filtered channel was paired with an unfiltered channel. Subtracting two filtered signals formed a Ross filter in which the signal difference represented energy bounded by the filter's K attenuation edge. Five data shots were collected per Ross filter and averaged. This average was divided by the integral of the average from the unfiltered channel to yield the mean fractional energy within a specific energy band. Each PMT was gated off-to-on for 5  $\mu$ s by a voltage pulse applied to the first and third dynodes of the tube. All PMT detectors were gated on 2  $\mu$ s prior to arrival of the x-ray pulse.



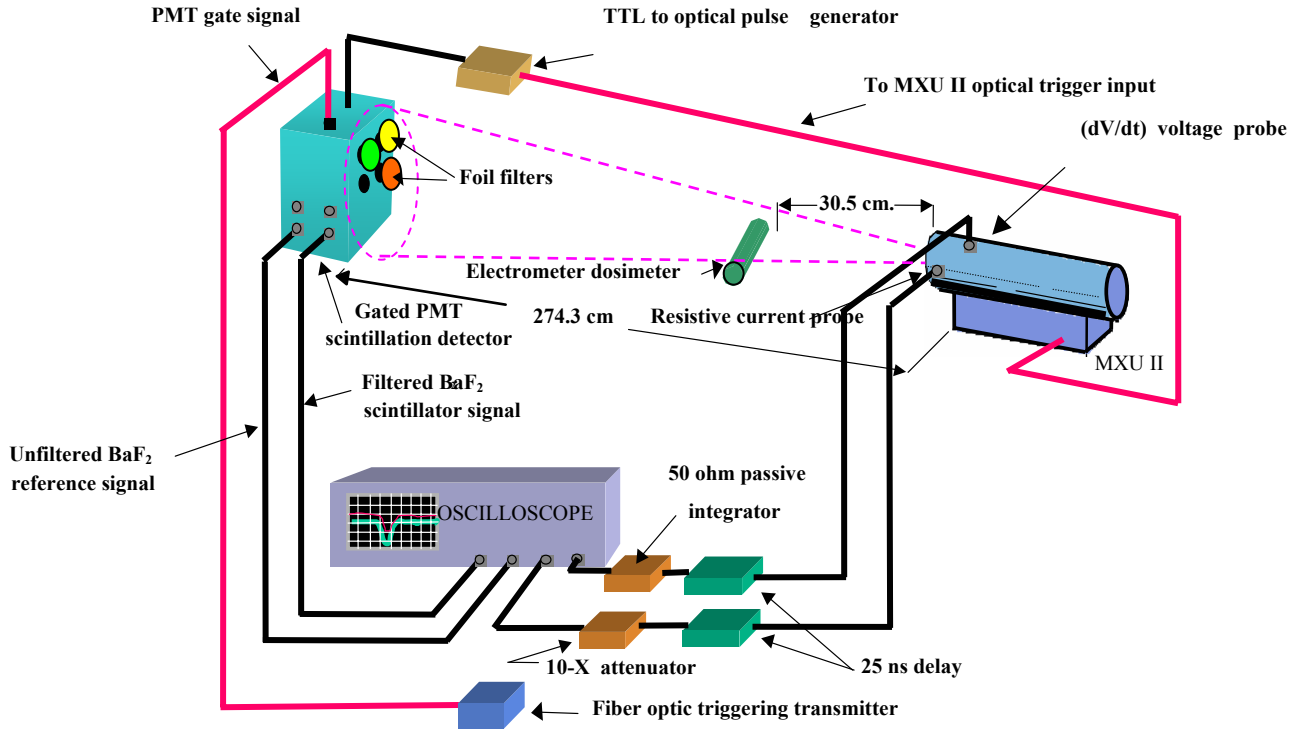


Fig. 7. Four-channel time resolved x-ray detector configured for wide band energy measurement.

Computation of the theoretical spectrum included filtration by the anode as well as filtration by the window of the x-ray tube. The spectrum algorithm assumes that only monoenergetic electrons strike the anode, and this previously has been shown to yield excellent agreement with measured data. In implementing this algorithm, the energy of the electrons which arrive at the anode are nonrelativistic and are proportional to the x-ray tube's AK potential. The electron number density scales as the ratio of the cathode current to the electron velocity, derived from the AK potential. The theoretical spectrum for the x-ray tube with a 2.5 mm AK gap is shown in Fig. 8. The spectrum was computed only for production of Bremsstrahlung radiation; the K-shell radiation from the Tungsten anode was not included in this computation.

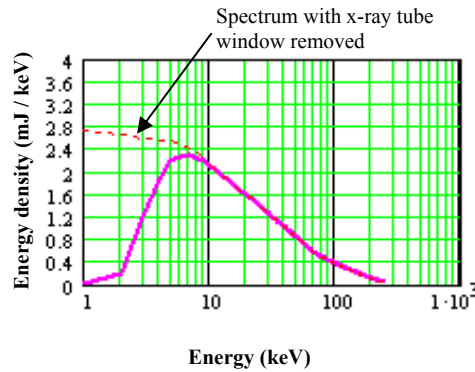


Fig. 8 Energy spectrum computed from simulated cathode current and AK voltage.

To compare the theoretical fraction of the total energy radiated within an energy band with the measured fraction, it was necessary to correct the theoretical fraction for the transmission response of the Ross filter. The measured and theoretical fractional energies in four energy bands are presented in Table 1. For x-ray energies above 67 keV, the agreement between theoretical and the experimental values is good. However, below 67 keV the disparity increases as the energy of the x-ray photon decreases. The measured energy fraction for 9-20 keV is almost  $\frac{1}{2}$  of the theoretical fraction. This difference is believed to result from absorption of radiation on the sputtered anode surface and suggests that the drop off and stabilization in the measured x-ray dose is just absorption of soft radiation at the anode surface. Another contribution to the theoretical energy fraction is the 59 keV Tungsten  $K_{\alpha 1,2}$  lines. Inclusion of these lines would increase the energy fraction in the 25-67 keV band. Additional inaccuracy in the simulated current and AK voltage would also contribute to errors in the calculated energy fraction.

Table 1. Comparison of the theoretical energy fraction and measured energy fraction.

Ross filter	Energy band (keV)	Theory	Measurement
30 $\mu$ m Cu - 10 $\mu$ m Mo	9-20 keV	0.021	0.012 $\pm$ .005
104 $\mu$ m Ta - 600 $\mu$ m Sn	25-67 keV	0.077	0.105 $\pm$ .003
112 $\mu$ m Pb - 104 $\mu$ m Ta	67-88 keV	0.064	0.076 $\pm$ .003
379 $\mu$ m Cu - 112 $\mu$ m Pb	$\geq$ 88 keV	0.106	0.105 $\pm$ .005

In summary, we demonstrated that SCL flow in x-ray tubes with conical anodes and coaxial cathodes can be successfully modeled using Langmuir's analytic solution for charge flow between coaxial cylinders, provided that the width of the plasma cathode is treated as a free parameter and that magnetic field effects can be neglected. The use of simulated cathode current and AK voltage has permitted a theoretical calculation of the x-ray emission spectrum, which was then used to calculate the fractional energy contained within designated energy bands. Comparing the theoretical with the measured energy fraction has confirmed that the x-ray tube is operating as a SCL diode and that the model can accurately simulate the emission spectrum and total radiated energy in the x-ray pulse. From the extrapolated time dependence of the AK gap it was determined that the moving plasma cathode, in a tube having a 2.5 mm AK gap, pinches until after the cathode current has passed through a first maximum. The subsequent rapid expansion of this cathode produces a secondary current maximum at a much lower AK voltage. Pinching of the plasma cathode is not the result of self magnetic fields because the cathode current is  $\ll 20$  kA, which is the threshold for pinched current flow in SCL diodes. The pinching of the plasma cathode is believed to be related to early emission from the high field corner at the rear of the cathode structure. This mode of tube operation generates an x-ray pulse with dual-energy characteristics, which is well suited for x-ray absorptometry measurements. The discrepancy between the theoretical

fractional energy and the measured fraction in the 9-20 keV and 25-67 keV bands can be partially attributed to x-rays emitted at low angles with respect to the anode surface and absorbed by sputtering features such as metal asperities and crater walls. In addition, the inclusion of the characteristic 59 keV K-shell emission from the Tungsten anode would further increase the fractional energy in the 25-67 keV band.

## **Results**

### **Digital Imaging of Organic Specimens**

System tests were run to evaluate the CT image capability of the software. The DEXA system was configured as shown in Fig. 1 to examine a Lamb femur. The proximal end of the femur was cut and appears horizontal in Fig. 9. The specimen was frozen to prevent motion during the periods between image collection, and the images were recorded on two stacked aSi digital panels and processed. The unprocessed image shown in Fig. 9 was acquired from the front panel, which is designed to be sensitive to 25-45 keV photons. Each image was processed using pixels located within a slice equivalent to a fan-beam. The set of all slices was processed to generate a volume view of the object capable of full 360 degree rotation about the x,y,z axis. Since hard and soft x-ray CT image data are available, DEXA can be used to extract both the density and composition of the scanned object. Specifically, the DEXA software uses a plastic-aluminum calibration phantom to create a raster of all possible values scanned, correlates this data to the correct attenuation value, generates a surface polynomial to approximate this surface, and then uses the surface to correct a complete dataset by simulating a monochromatic source. When the corrected dataset is passed through a CT 3D reconstruction, the resulting reconstruction contains calibrated data that can be used to determine the volumetric density.

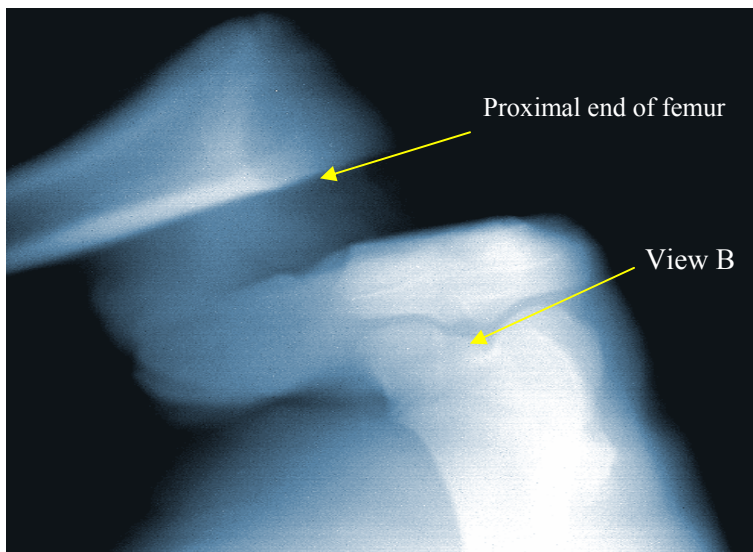


Fig. 9 Single image of a Lamb Femur. Front imaging panel 25-45 keV, 0.45 m source to object distance, and <23 mrad exposure.

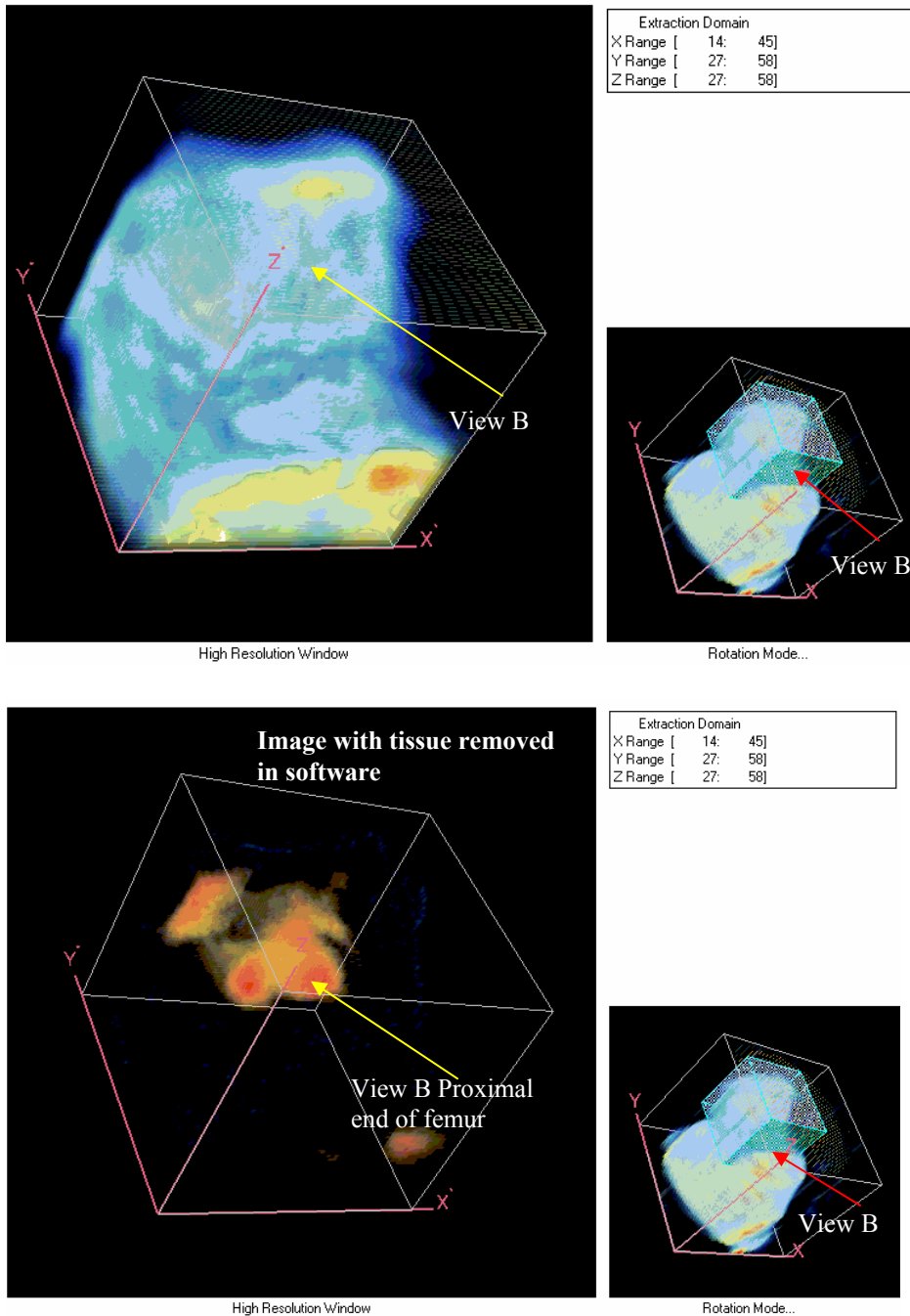


Fig. 10. 3D representations of the portion of Fig. 9 labeled View B.

The images in Fig. 10 demonstrate that it is possible to extract the denser bone-mineral from the surrounding tissue by applying a cubic volume opacity filter followed by an isosurface reconstruction of the digitized x-ray image. By using both soft (25-45 keV) and hard (67-150 keV) images, the bone mineral density in the CT volume reconstruction can be determined.

## **CONCLUSION**

Understanding the process of charge flow in Marx driven x-ray tubes has been one of the goals of this research. The SCL flow in x-ray tubes with conical anodes and coaxial cathodes has been successfully modeled using Langmuir's analytic solution for charge flow between coaxial cylinders, provided that the width of the plasma cathode is treated as a free parameter and that magnetic field effects can be neglected.

The use of simulated cathode current and AK voltage in a calculation of the x-ray emission spectrum has confirmed that the x-ray tube is operating as a SCL diode and that our model can accurately simulate the emission spectrum and total radiated energy in the x-ray pulse. Moreover it has been shown that when the filtered hard x-ray pulse is subtracted from the unfiltered x-ray pulse, the residual pulse is the expected soft x-ray pulse with the correct temporal shape. That is, the soft x-ray pulse occurs later in time after the voltage has peaked in the x-ray tube. This work experimentally verifies the dual-energy nature of the x-ray pulse.

The second research goal was to develop a digital imaging system with radiography and computed tomography (CT) capabilities. The ability of the present system to deliver detailed CT volume reconstructions is dependent on the number of views in the sampling set. The excellent resolution in individual images is due to the small diameter, <3 mm, of the x-ray emission spot. The digital images obtained to date, and used to generate 3D volume reconstructions of biologic specimens, are not constrained by hardware or software limitations but by the number of views in the sample. The present system has the necessary software to determine the bone mineral density of specific volumetric sites within the specimen.

## **Presentations**

“Dual-Energy X-Ray System for Bone Mineral Densitometry and Diagnostic Radiography,” Bioastronautics Investigator’s Workshop, 17-19 January 2001, Galveston.

“Intense Source of Nanosecond Duration X-Rays in the 10 keV to 250 keV Range for Diagnostic and Medical Radiography Applications,” S.P.I.E. Annual Meeting, 7-11 July 2002, Seattle.

“Dual-Energy X-Ray CAT System for Precision Bone Mineral Densitometry and Diagnostic Radiography,” Bioastronautics Investigator’s Workshop, 13-15 January 2003, Galveston.

## **Patents**

“Field Emission Tube for a Mobile X-Ray Unit,” Patent No. 6064718 issued 16 May 2000.

“Capacitor Mounting Arrangement for Marx Generators,” Patent No. 6166459 issued 26 December 2000.

“Mobile X-Ray Unit,” Patent No. 6205200 issued 20 March 2001.

“Dual Energy Detector,” Patent Application 09-419-261.